JOURNAL OF GEOPHYSICAL RESEARCH, VOL. 112, B06312, doi:10.1029/2006JB004382, 2007

Click Here for Full Article

Imaging of crustal heterogeneous structures using a slowness-weighted back-projection with effects of scattering modes: 2. Application to the Nagamachi-Rifu fault, Japan, area

T. Taira,[1,2] K. Yomogida,[1] Y. Kuwahara,[3] K. Imanishi,[3] and H. Ito[3,4]

Received 7 March 2006; revised 11 November 2006; accepted 13 February 2007; published 27 June 2007.

[1] This is the second paper in a two-part series on a newly developed imaging approach for small-scale heterogeneities (<1 km) in the crust with effects of scattering modes. In the present paper, we estimated a detail three-dimensional spatial distribution of small-scale heterogeneities around the Nagamachi-Rifu fault, northeastern Japan, in a frequency range of 2–16 Hz, using the imaging approach presented in the first paper. We used seismograms recorded by dense three-component seismic arrays that were deployed in this region for 15 explosion sources. As one of our important results, there are concentrations for only *P-S* but not *P-P* scatterers near the surface trace of the fault. *P-S* scatterers in a frequency range of 8–16 Hz are localized near the surface trace of the fault, implying the possibility of strong heterogeneities with a size of 0.08 km there. In the Shirasawa caldera region, the characteristics of seismic scatterers seem to convert from large *P-S* to large *P-P* relative scattering coefficients with its transition depth range of 5–8 km. This feature implies that the materials composed of seismic scatterers may show a systematic variation with depth. Finally, the strength of scattering coefficients is rather weak in the coseismic area of the 15 September 1998 earthquake with a magnitude of 5.2, the largest recent event in this area. This result suggests that this coseismic area is rather homogeneous and can hold local stress larger than in the surrounding portions of the fault system.

Citation: Taira, T., K. Yomogida, Y. Kuwahara, K. Imanishi, and H. Ito (2007), Imaging of crustal heterogeneous structures using a slowness-weighted back-projection with effects of scattering modes: 2. Application to the Nagamachi-Rifu fault, Japan, area, *J. Geophys. Res.*, *112*, B06312, doi:10.1029/2006JB004382.

1. Introduction

[2] Small-scale heterogeneities in the crust and upper mantle play an important role in understanding the nucleation process of earthquakes, particularly their scale lengths less than several kilometers. Analyses of high-frequency (>1 Hz) *P*- and *S*-coda waves have retrieved distributions and characteristics of small-scale heterogeneities [e.g., *Aki*, 1973; *Capon*, 1974; *Aki*, 1982; *Wu and Aki*, 1985]. Appropriate methods for determining properties of small-scale heterogeneities are summarized in Figure 13.11 of *Aki and Richards* [1980].

[3] The density and scale of regional seismic observations have been improved significantly for the last decade, so that we are currently in the stage that we can obtain the overall spatial distribution of small-scale heterogeneities in the crust or upper mantle accurately and stably. Many studies have recently revealed heterogeneous structures in the crust [e.g., *Nishigami*, 2000; *Revenaugh*, 2000], the subduction zone [e.g., *Revenaugh*, 1995; *Louie et al.*, 2002; *Taira and Yomogida*, 2004], and the upper mantle [e.g., *Frederiksen and Revenaugh*, 2004].

[4] For example, *Rondenay et al.* [2001] estimated two-dimensional heterogeneous structures as *P* and *S* velocity perturbations from a reference model across the Cascadia subduction zone offshore in central Oregon, the United States, using the Born-approximate inversion of scattered teleseismic waves. They found a low-velocity layer in both *P* and *S* velocity perturbations with a dip of about 10° to the east from 20 km to 40 km depth. They suggested that this layer is associated with the oceanic crust of the subducting Juan de Fuca plate beneath the Coast Ranges of Oregon, interpreting a layer due to metamorphic dehydration reactions in the oceanic crust.

[5] Another approach for estimating spatial locations of seismic scatterers is based on seismic array techniques such as a frequency-wave number (*f-k*) [e.g., *Capon*, 1969],

[1]Division of Earth and Planetary Sciences, Graduate School of Science, Hokkaido University, Sapporo, Japan.
[2]Now at Department of Terrestrial Magnetism, Carnegie Institution of Washington, Washington, D. C., USA.
[3]Geological Survey of Japan, National Institute of Advanced Industrial Science and Technology, Tsukuba, Japan.
[4]Now at Center for Deep Earth Exploration, Japan Agency for Marine-Earth Science and Technology, Yokohama, Japan.

Copyright 2007 by the American Geophysical Union.
0148-0227/07/2006JB004382$09.00

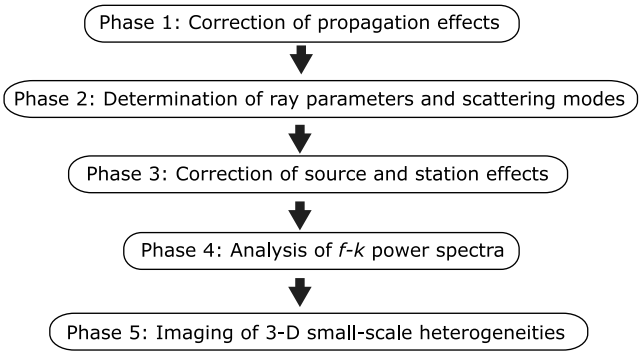

Figure 1. Flowchart of the imaging procedure presented by *Taira and Yomogida* [2007]. The imaging procedure is classified into five phases.

semblance analysis [e.g., *Neidell and Taner*, 1971], and zero-lag cross-correlation [e.g., *Frankel et al.*, 1991]. These techniques define scattering points as deterministic secondary sources based on coherencies of scattered phases, parameterizing specific scattering strengths by using *f-k* powers, semblance values, and cross-correlation coefficients as a function of space.

[6] Several enhanced seismic array techniques have been recently introduced and widely applied for determination of seismic scatterers locations [e.g., *Spudich and Bostwick*, 1987; *Bannister et al.*, 1990; *Scherbaum et al.*, 1997; *Kaneshima and Helffrich*, 1998; *Rietbrock and Scherbaum*, 1999; *Rothert and Ritter*, 2001]. *Krüger et al.* [1993] proposed a new seismic array technique, named double beamforming, utilizing beamformings from both source and station arrays. They identified anomalous arrivals as *PcP* precursors in the seismograms recorded by the Yellowknife array, Canada, suggesting that these arrivals are caused by heterogeneities of the lowermost mantle in Severnaya Zemlya, Russian arctic.

[7] *Taira and Yomogida* [2007] (hereafter called Paper I) developed a newly imaging approach for spatial distributions of small-scale heterogeneities in the crust as seismic scatterers with a three-component (3-C) seismic array data. This imaging approach incorporates both *f-k* and polarization analyses, in order to not only enhance weak scattered phases but also determine their scattering modes (i.e., *P-P* or *P-S* for explosion seismograms). In addition, the imaging approach applies a polynomial regression model, based on a stationary autoregressive (AR) model to the temporal decay of each seismogram, in order to remove various kinds of constraints of propagation effects (e.g., a representation of attenuation factor). On the other hand, source and station effects are removed in each frequency range by the coda-normalization method. Locations of seismic scatterers are estimated accurately, by using travel times together with slowness vectors for a three-dimensional velocity structure. Figure 1 summarizes the procedure of the imaging approach proposed by Paper I.

[8] In this paper, the imaging approach developed in Paper I is applied to 3-C seismograms recorded by small-aperture arrays deployed in the Nagamachi-Rifu fault (NRF) region, running through the middle of Sendai City in northeastern Japan. Our images of seismic scatterers turn to have the following points superior to the previous results of imaging small-scale heterogeneities: (1) three-dimensional distributions with good spatial resolution, (2) images at various frequencies, that is, distribution of different scale lengths, and (3) individual images of *P-P* and *P-S* scatterings. Taking these advantages, we shall discuss the nature of heterogeneous structures as seismic scatterers in this region in a quantitative manner. For example, we attempt to discuss seismological and tectonic implications of imaged heterogeneities in areas such as (1) along the NRF system, (2) the Shirasawa caldera region, and (3) the coseismic area of the 15 September 1998 moderate earthquake.

2. Tectonic Setting and Data

2.1. Tectonic Setting

[9] The NRF is an active reverse fault with a strike of northeast-southwest, which is running through the middle of the urban area of Sendai City, northeastern Japan. Its past activity has been investigated, based on its topographic and geologic surveys. *Active Fault Research Group* [1991] evaluated that its average slip rate is $0.6-1.0 \times 10^{-3}$ km/ka. The NRF is assessed by its local prefectural government with the potential to produce a destructive earthquake of magnitude 7 in the future [*Miyagi Prefectural Government*, 1997].

[10] The crustal structure of the Sendai urban area is mainly controlled by three Neogene tectonic events, that is, (1) extensional deformation in early Miocene, (2) formation of calderas in late Miocene, and (3) final shorting deformation since late Pliocene [e.g., *Sato*, 1994; *Sato et al.*, 2002]. Well-developed calderas in the stage of (2) that have been collapsed since then are also distributed in the western part of Sendai city, particularly in late Cenozoic [*Yoshida*, 2001]. Owing to regional compressional stress trending in WNW-ESE since late Pliocene (i.e., event 3 above), the normal faults formed in Miocene (i.e., event 1) have been reactivated as reverse faults. Figure 2a shows one of the standard geological structures of NE Japan complied by *Sato* [1994].

[11] A temporary seismic observation around the NRF from October 1996 to March 1998 showed that somewhat concentrated microearthquake activities were identified in the hanging wall side of the NRF [*Yoshimoto et al.*, 2000]. These microearthquakes, distributed not exactly on the fault plane but in the hanging wall side of the fault with some extent, have either reverse-fault type or strike-slip fault type focal mechanism with nearly horizontal *P* axis of the strike of NW-SE.

[12] An earthquake with magnitude of 5.2 in the Japan Meteorological Agency Magnitude occurred beneath the Ayashi area of the city on 15 September 1998 (Figure 2a) (hereafter called the 1998 M_j 5.2 earthquake). Its hypocenter locates at about 12 km depth and approximately 10 km to the northwest of the surface trace of the NRF [e.g., *Umino et al.*, 2002a]. Its focal mechanism determined by *P*-wave polarity data is a reverse-fault type with nearly horizontal *P*-axis in the NW-SE direction. The focal mechanism, together with the relative location of the surface trace of the NRF to the fault plane of the 1998 M_j 5.2 earthquake, suggests that this event ruptured the deepest portion of the fault [*Umino et al.*, 2002a].

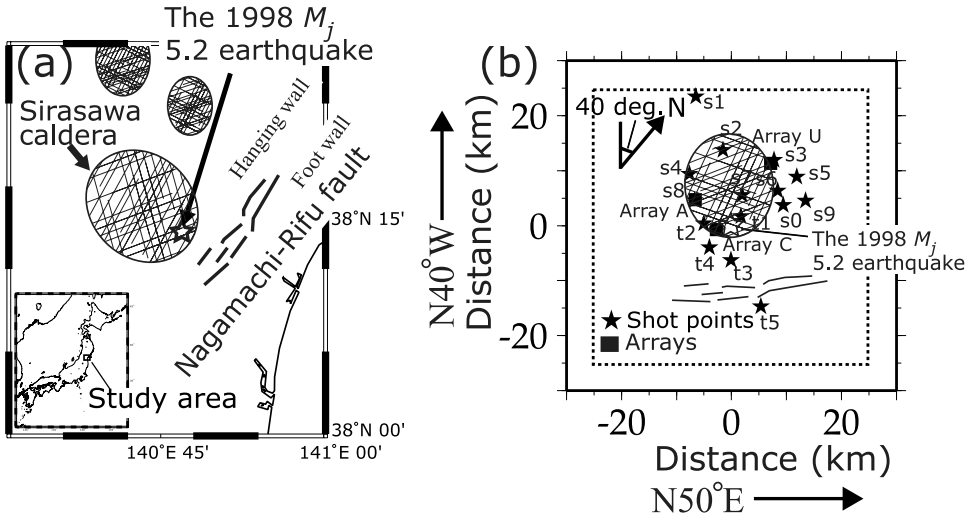

Figure 2. (a) Map of active faults (solid lines), calderas (hatched ovals), and the epicenter of the 1998 M_j 5.2 earthquake (open star). The locations of calderas are based on work by *Sato* [1994]. (b) Distribution of arrays (solid squares) and shotpoints (solid stars) used in this study. The coordinate center is located at the epicenter of the 1998 M_j 5.2 earthquake shown by the large open star in Figure 2a, and the coordinate system is rotated anticlockwise by 40°. The dashed square indicates the model space for estimating locations of scattering coefficients: 50 km × 50 km in horizontal and 18 km in depth (−1 km to 17 km).

[13] *Umino et al.* [2002b] revealed the locations and the properties of *S*-wave reflectors from clear $S \times S$ phases (i.e., *S*-*S* reflected phases), by using spectral amplitude ratios of $S \times S$ phases to direct *S*-waves beneath the NRF. They estimated that clear seismic reflectors are located in the depth range from 15 km to 21 km, just beneath the fault plane of the 1998 M_j 5.2 earthquake. They also estimated the *S*-wave velocity and thickness of the reflector to be about 1.0 km/s and 0.05 km, respectively. They concluded that the reflector is filled with fluid, probably H_2O. *Nakajima et al.* [2006] estimated that a zone of large V_p/V_s ratio is located from the lower crust to the uppermost mantle, just below the hanging wall side of the NRF, using their three-dimensional seismic tomography technique. They also suggested that this large V_p/V_s zone is caused by the existence of partially melted materials. Since the spatial variation of velocity fluctuations such as V_p/V_s depends strongly on the distribution of small-scale heterogeneities, it is important to investigate a detail nature of small-scale heterogeneities, in order to understand the generation mechanism of inland earthquakes.

2.2. Experiment and Data

[14] Seismic reflection/refraction experiments around the NRF were conducted as a part of the comprehensive joint research project named Modeling of Deep Slip Processes in Seismogenic Inland Faults. The purpose of the experiments was mainly the investigation of deep structures of the NRF and its relation with the 1998 M_j 5.2 earthquake. These intensive experiments included active and passive recordings of chemical explosions, truck mounted vibrators, and natural earthquakes during a three-day period in June 2001. The detail of these experiments was described by *Hasegawa et al.* [2001]. In these experiments, a group, named the Research Group for Deep Structure of Nagamachi-Rifu fault, set up a dense 3-C seismic array (named array U) in the north of the hypocenter of the 1998 M_j 5.2 earthquake [*Nakamura et al.*, 2002]. Geological Survey of Japan, National Institute of Advanced Industrial Science and Technology (GSJ, AIST) also carried out four small aperture seismic arrays (named arrays from A to D) around the NRF [*Imanishi et al.*, 2002]. In this study, we use the seismograms recorded by three arrays: U, A, and C for the 15 explosion sources (Figure 2b and Table 1). An example of 8–16 Hz bandpass filtered seismograms is shown in Figure 3, for shot s2 at array U.

[15] Array U consisted of 60 short-period 3-C seismometers, Mark Products Inc. L28-B (with the natural frequency of 4.5 Hz), with about 0.05 km interval. Off-line data recording systems with LS8000 loggers (Hakusan Co.) recorded seismic signals from each vibrator or chemical explosion at the sampling rate of 100 Hz. On the other hand, each of arrays A and C consisted of 32 3-C seismic stations with the 0.02-km spacing. Their sensors were 2 Hz L22E (Mark Products Inc.) short-period seismometers and the sampling frequency of recorders was 500 Hz. Figure 4 shows geometrical configurations and array response functions of arrays U, A, and C. These array response functions were determined by their array geometries, and they are not delta-function like but show some spatial extents. The spatial resolution of array response in array U is better than one in array A or C (Figure 4c), because the total length of array U is the longest. The array response of array U is very close to a delta function. On the other hand, the longest station spacing of the three arrays was about 0.05 km, so we are able to determine *f*-*k* power spectra with a wavelength of about 0.1 km, much smaller than the block size (3 km × 3 km × 3 km) used for determining the locations of scatterers in the next section.

Table 1. Shot Times, Locations, and Charge Sizes of 15 Explosion Sources in the 2001 Seismic Experiment[a]

Shot Number	Date	Shot Time, JST[b]	Latitude, °N	Longitude, °E	Altitude, km	Charge, kg
s0	18 June	02:16:00.016	38.3586	140.8130	0.184	100
s1	16 June	01:01:00.000	38.4026	140.5281	0.355	100
s2	16 June	00:01:00.022	38.3636	140.6431	0.442	130
s3	18 June	01:26:00.015	38.4053	140.7378	0.439	100
s4	16 June	00:31:00.049	38.2982	140.6217	0.289	100
s5	18 June	00:31:00.000	38.4080	140.7964	0.164	100
s6	18 June	00:01:00.001	38.3704	140.7845	0.160	100
s7	16 June	01:31:00.039	38.3279	140.7340	0.273	70
s8	16 June	02:01:00.016	38.2710	140.6652	0.218	100
s9	18 June	02:01:00.029	38.3873	140.8426	0.076	100
t1	17 June	01:31:00.030	38.2995	140.7604	0.156	100
t2	17 June	02:06:00.027	38.2513	140.7111	0.184	100
t3	17 June	00:01:00.009	38.2342	140.8030	0.147	100
t4	17 June	00:31:00.043	38.2276	140.7516	0.132	100
t5	17 June	01:01:00.055	38.2077	140.9128	0.004	100

[a]Modified from *Research Group for Deep Structure of Nagamachi-Rifu Fault* [2002].
[b]Japanese standard time.

[16] As the very first step of our data analysis, we correct the response of the recording systems, and then obtain displacement seismograms. Spatial aliasing appears in these array configurations for any scattered waves at frequency higher than 20 Hz because of the limitation originated from the station spacing of the arrays (0.05 km) to be nearly equal to their aliasing wavelengths, assuming the shear wave velocity to be 1.96 km/s [*Imanishi et al.*, 2002]. On one hand, the contribution of background noise or incoherent signals in the present data set is generally larger than one of coherent signals at frequency lower than 2 Hz, mainly owing to the lower limit of the sensitivity range of recording systems. For this reason, the above displacement seismograms are then band-pass filtered in a frequency range between 2 Hz and 16 Hz, as a frequency range of good quality, for further analyses. We only analyze the displacement seismograms where the signal-to-noise ratio is greater than 2.

3. Imaging of Small-Scale Heterogeneous Structure

3.1. Data Analysis

[17] In this section, we apply the imaging method proposed by Paper I, in order to estimate the spatial distribution of small-scale heterogeneities as seismic scatterers, following the procedures in Figure 1. In Phase 1, we correct the overall propagation effect including anelastic attenuation by so-called ''amplitude recovery'', by applying the polynomial regression fitting with the Akaike Information Criterion (AIC) approach. Figure 5a shows the 3-C seismogram for shot s2 at station 6042 after the correction of the overall propagation effect. In this study, most of the envelopes recorded by array U show AIC(M) values to be minimum with around M = 12, where M indicates the optimal polynomial order of the regression coefficients (see Paper I). In order to evaluate reliable scattering coefficients, we additionally correct the background effect of scattering attenuation. Since we apply a general polynomial model (i.e., a product of up to n-th order exponentials) to the data set in amplitude recovery, any scattering effects in the background medium can be removed in the present data processing of amplitude recovery, as long as they are not much larger than the effect of anelastic attenuation along each propagation path (i.e., multiple scattering not dominant over single scattering).

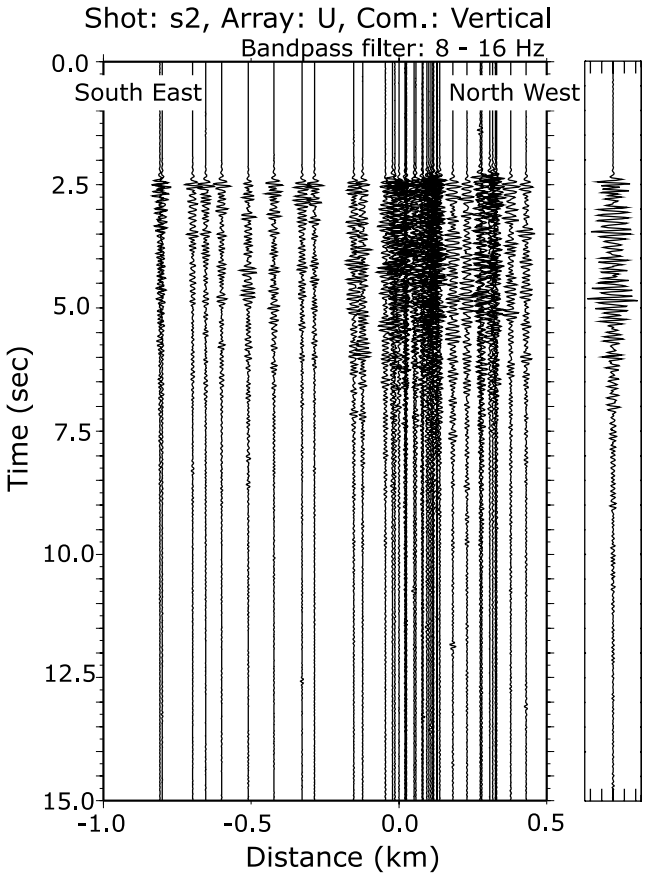

Figure 3. (left) Example of bandpass filtered (8–16 Hz) seismograms for shot s2 at vertical component of array U. Traces are aligned across the NRF and arranged by distance from the reference station (station 6042). (right) Enlarged view of the seismogram at the reference station.

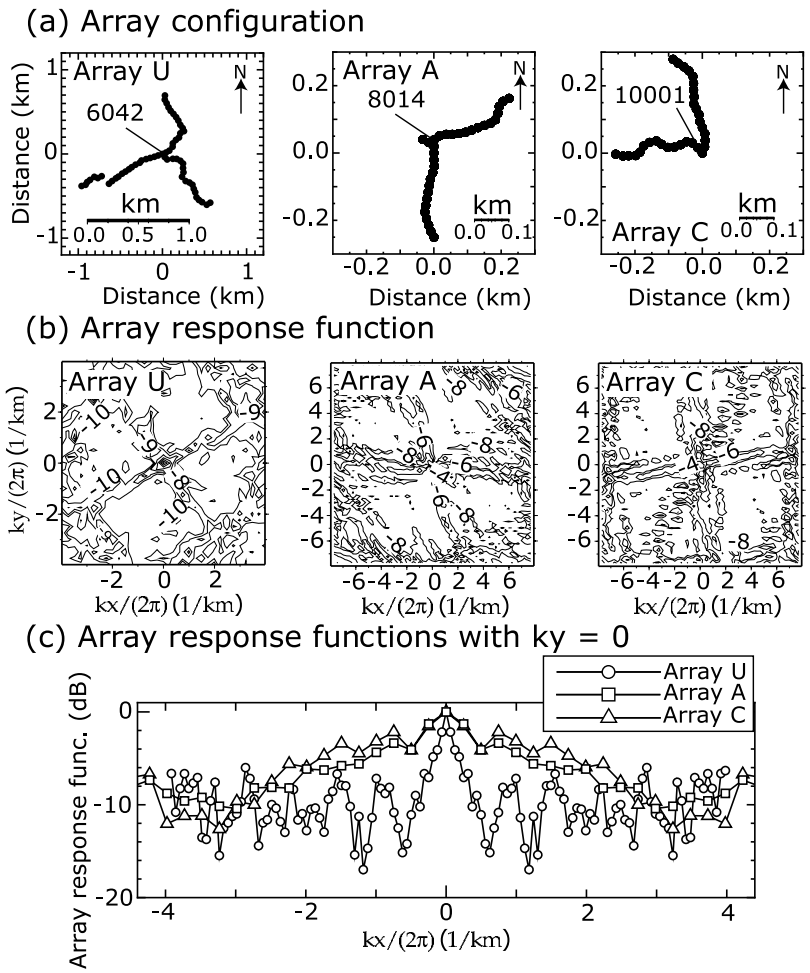

Figure 4. (a) Array configurations and (b) array response functions of arrays U, A, and C. The maximum value in Figure 4b is normalized to be 0 dB. (c) Array response functions as a function of k_x with $k_y = 0$. Circles, squares, and triangles represent array response functions of arrays U, A, and C, respectively.

[18] In Phase 2, both ray parameter and scattering mode of each scattered wave are determined. We first determine the 2-D slowness vector (i.e., the apparent velocity v_{app} and arrival direction θ) and the dominant frequency f of each scattered wave, using the *f-k* analysis with a stationary AR model. The *f-k* power spectra are obtained with 0.32-s windows sliding with the increment of 0.08 s through each entire record. The slowness domain spans a range of up to 0.512 s/km with the sampling interval of 0.016 s/km. In order to reduce ambient noise, *f-k* power spectra are stacked in three frequency ranges; 2–4 Hz, 4–8 Hz and 8–16 Hz. Next, polarization vectors (i.e., azimuth Θ_H and dip Θ_V of the maximum polarization) and the degree of elliptical polarization P_E are estimated by performing the polarization analysis with a stationary multivariate autoregressive (MAR) model (Figure 5b). Note that P_E becomes 0 for a perfect linear polarization. To enhance signal-to-noise ratio, polarization characteristics are evaluated from stacked covariance matrices, using all the stations of each array. Using the same window length and time increment value as the *f-k* analysis, the covariance matrices are computed from seismograms aligned by the delay time with the maximum *f-k* power in each time window.

[19] Incorporating the observed slowness and polarization vectors, wave types of scattered waves are finally identified, based on the following steps. Using the estimated apparent velocity, v_{app}, of each scattered wave, surface waves are first excluded from our data set. In this study, the *S*-wave velocity of the first layer is set to be 1.96 km/s, based on the *P*-wave velocity (3.40 km/s) of the layer in the NRF estimated by *Imanishi et al.* [2002], assuming the Poisson's ratio to be $\sqrt{3}$. Scattered waves with v_{app} less than 1.96 km/s are removed from the data set, and the rest of scattered waves are classified into the two categories based on their apparent velocities: (1) $3.40 < v_{app}$ for *P-P* or *P-S* wave and (2) $1.96 \leq v_{app} \leq 3.40$ for *P-S* wave. Next, the scattered waves for the category 1 are distinguished into *P-P* wave and *P-S* wave, and those for the category 2 are examined to confirm the estimated polarization to be consistent with that of *S* wave. In order to verify the wave-type of scattered waves in each category, we compute the angle, Ψ, between the 3-D slowness and polarization vectors. This angle Ψ are set to take a range from 0° to 90°. Note that 3-D slowness vectors are determined from 2-D ones, assuming the surface layer velocities for *S*- and *P*-waves. Note also that we

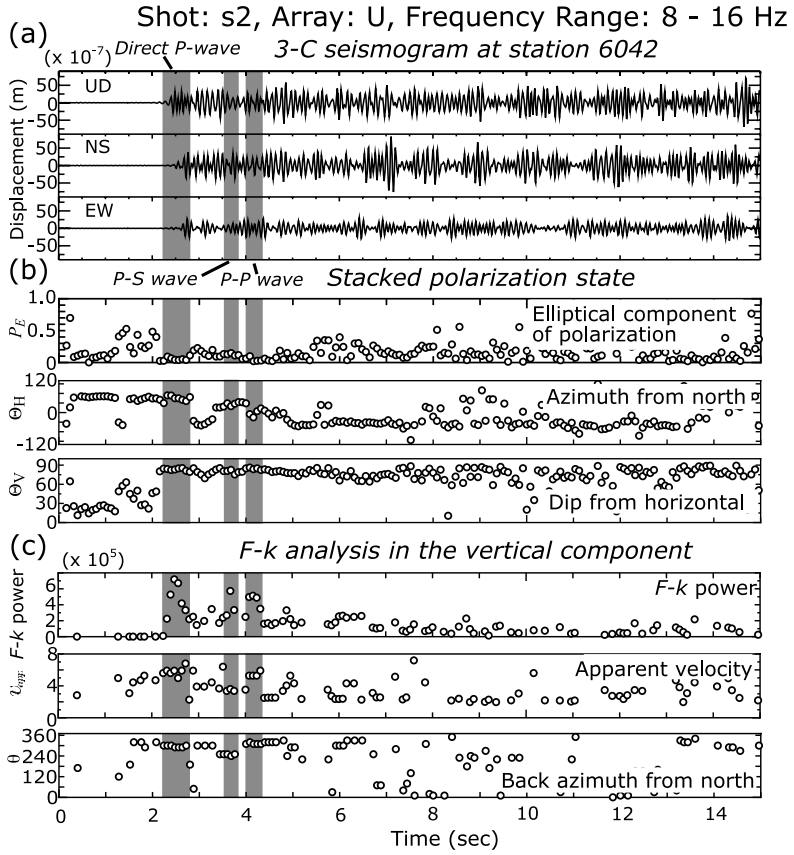

Figure 5. Results for polarization and *f-k* analyses in a frequency range of 8–16 Hz for the example of Figure 3. (a) The 3-C component seismogram for shot s2 at station 6042 after bandpass filtered (8–16 Hz) and the correction of overall propagation effects. (b) Stacked polarization state: (top) elliptical component of polarization, (middle) strike from north, and (bottom) dip from the ground surface. (c) Result for *f-k* analysis in the vertical component after the correction of source and station effects: (top) *f-k* power, (middle) apparent velocity, and (bottom) back azimuth from north. Three arrivals in shaded zones are identified as the direct *P*-wave and two later phases.

estimate two angles for *P-P* and *P-S* waves (i.e., Ψ_p and Ψ_s) in the category 1.

[20] We here define the credibility of wave-type in the forms of $C_p = 90 - \Psi_p$ in degree for *P* wave and $C_s = \Psi_s$ for *S* wave. To enhance our data quality, the scattered waves with *C* less than 45 are excluded from the data set. After sorting by the credibility of wave-type in the category 2, the rest of the scattered waves are thus identified as *S* wave. For the category 1, if $C_s < C_p$, such a scattered wave is identified as *P* wave while *S* wave for $C_p \leq C_s$.

[21] In addition to the credibility of wave-type, we take into account the degree of elliptical polarization P_E to confirm the reliability of our classification of scattered waves. In this study, we define that the upper limit of P_E is to be 0.4. This threshold value of P_E is determined based on an numerical experiment with waveforms containing incoherent noise (see Paper I). We apply the above steps to the entire data set for all the source-station (i.e., array) pairs.

[22] As Phase 3, we perform the coda-normalization method to correct source and station effects. We here consider seismic-source radiation and surface geology just beneath stations as source and station effects, respectively. They particularly affect on amplitudes of high-frequency seismograms [e.g., *Sato and Fehler*, 1998] as explained in Paper I in detail. We minimize these two effects on an individual seismogram, by taking the spectral amplitude ratio of the early to later coda parts. The early coda part can be assumed to contain coherent scattered phases from individual scatterers [e.g., *Spudich and Bostwick*, 1987] while the later coda part can consist of scattered phases from scatterers distributed over a large volume surrounding stations and sources [e.g., *Aki*, 1969].

[23] We define the early coda part starting with a lapse time after 0.32 s from the *P*-wave travel time and its time window to be 15 s. The time window of the later coda part is set to be 5.12 s after the early coda part. We first compute spectral amplitudes of both coda parts, and then normalize the amplitude spectrum of the early coda part by one of the later coda part. Effects of seismic-source radiation and surface geology of the early coda part can be common for the later coda part among different stations and sources [*Sato and Fehler*, 1998]. Source and station effects can therefore be removed through the above normalization procedure. We finally obtain normalized seismograms after this correction of source and station effects by the inverse Fourier transform of the normalized spectra. We assume explosion-source radiation patterns to be isotropic.

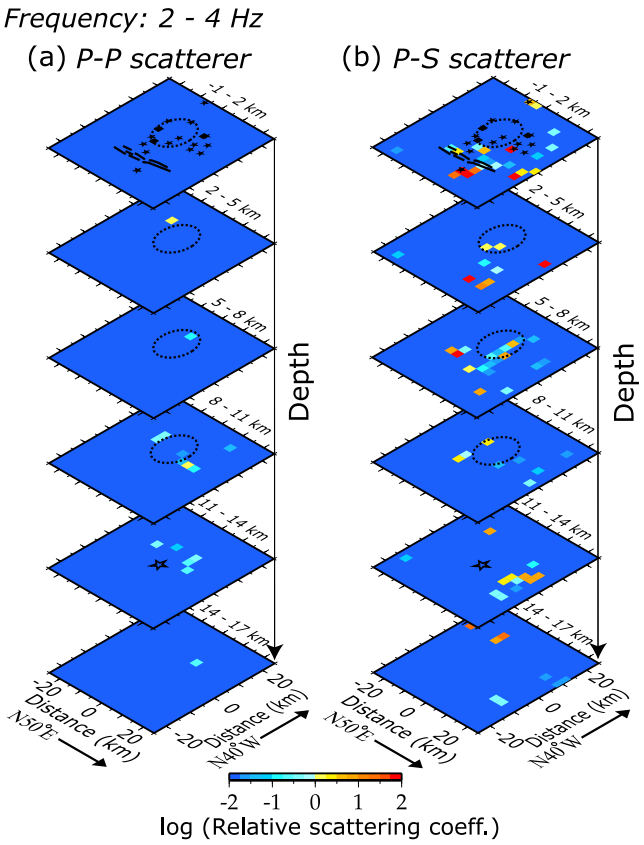

Figure 6. Depth slices of the distributions of scattering coefficients for (a) *P-P* and (b) *P-S* scatterers for our data set in a frequency range of 2–4 Hz. The magnitude of each relative scattering coefficient is shown by the color bar, as shown at the bottom. Solid stars and squares denote shot and array locations, respectively. Open star, black lines, and dashed ovals indicate the hypocenter of the 1998 M_j 5.2 earthquake, the surface trace of the NRF system, and the Shirasawa caldera region, respectively.

[24] Among all the stations of a given array, we picked coherent scattered waves by our *f-k* analysis. The sizes of our arrays were small enough to identify such coherent waves even in high frequency (>1 Hz). This was also confirmed by the analysis of direct *P*-waves (see Paper I). We therefore need not to consider effects of phase shifts due to surface geology.

[25] After corrections, in Phase 4, *f-k* power spectra are calculated again with the same time window in the former *f-k* analysis of Phase 2, using the total record length of 15 s responsible for the arrival range of scattered waves (Figure 5c).

[26] As Phase 5, we estimate the 3-D distribution of small-scale heterogeneities around the NRF, by applying the slowness-weighted back-projection method to the normalized seismograms. The extent of the model space is shown in Figure 2b, that is, 50 km × 50 km in horizontal and 18 km in depth. In this study, each heterogeneity is expressed as a value of scattering coefficient inferred from the *f-k* power spectrum located at each block of the volume δV. We select the volume of each block δV to be 3 km × 3 km × 3 km. This scattering coefficient represents the strength of scatterers distributed in a medium. Note that we only consider the maximum *f-k* power corresponding to the dominant scattered wavefield. In order to constrain possible blocks as the locations of distinguished scatterers, we compute the fit function between the observed and calculated travel times as well as slowness vectors of the *p*-th block in the form of $f(p) = \exp(-(\tau^{obs} - \tau^{cal})^2/2\sigma_\tau^2) \cdot \exp(-(\mathbf{s}^{obs} - \mathbf{s}^{cal})^2/2\sigma_\mathbf{s}^2)$, where τ and $\mathbf{s}$ are the travel time and slowness vector, respectively. σ_τ and $\sigma_\mathbf{s}$ indicate the standard deviations in the estimations of travel time and slowness vector, respectively, so that errors in the estimations of travel time and slowness vector is evaluated by using the introduced fit function. In this study, σ_τ and $\sigma_\mathbf{s}$ are set to be 0.32 and 0.016. Using this fit function, we define the possible block p^{sca} where the fit function value is greater than 0.95 or $p^{sca} = \{p | f(p) > 0.95\}$. We can measure errors in locations of scatterers based on areas where fit function values are grater than 0.95. This threshold value is determined through the numerical experiments described in Appendix A so that not only the assigned scatterers can be recovered well but also artifacts can be suppressed sufficiently.

[27] In order to obtain the reliable location of each scatterer, it is furthermore desirable to use the information of seismic 3-D velocity structure, compared with simple homogeneous or 1-D velocity structure that has been used the previous studies. We use the 3-D seismic velocity structure model, obtained by the travel time tomographic study of *Nakajima et al.* [2006], for the calculation of raypath and travel time from a given source to a given station via each scatterer or model block, based on the pseudo-bending method [*Um and Thurber*, 1987].

[28] For horizontal component data, the majority of the present horizontal *f-k* power spectrograms are composed of surface waves inferred from their apparent velocities smaller than the *S*-wave velocity of the first layer (1.96 km/s). We therefore focus on vertical *f-k* spectrograms with apparent velocity larger than the *S*-wave velocity of the first layer, as scattered body waves to be imaged, in order to estimate the distribution of scattering coefficients. It is better to emphasize that horizontal components are nevertheless useful in this study because they are essential in the determination of the scattering mode (*P-P* or *P-S*) of each phase by the polarization analysis.

3.2. Results and Numerical Experiment

[29] Following the procedures explained in section 3.1, we obtained the 3-D image sections of scattering coefficients around the NRF, in three frequency ranges of 2–4 Hz, 4–8 Hz, and 8–16 Hz for *P-P* and *P-S* scatterings separately. Figures 6, 7, and 8 show depth slices of the distributions of scattering coefficients for *P-P* and *P-S* scatterers in frequency ranges of 2–4 Hz, 4–8 Hz, and 8–16 Hz, respectively. Note that we show the scatterers detected by at least two shot-array pairs, in order to ensure the obtained image sections. Note also that *P-P* and *P-S* scattering coefficients in all the frequency ranges are normalized by a common value, and are shown in log scale.

[30] The obtained image sections of *P-P* and *P-S* scattering coefficients (Figures 6, 7, and 8) clearly show nonuniform spatial distributions of small-scale heterogeneities around the NRF. Focusing on the fault zone, one of the

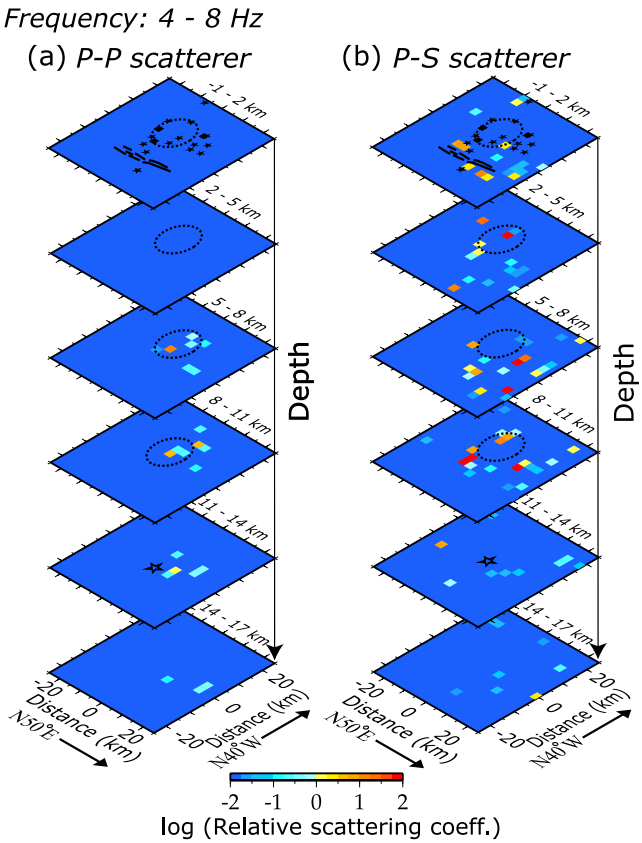

Figure 7. Same as Figure 6 except for 4–8 Hz.

most remarkable features in the obtained distributions of scattering coefficients is the dominance of *P-S* scattering. This feature is consistent with the response expected from a theoretical analysis of the properties of scatterers [*Aki*, 1992]. The seismic reflection profile obtained in this zone [*Ikawa et al.*, 2001] indeed supports the existence an area with highly concentrated small-scale heterogeneities at depth shallower than 10 km.

[31] Using the retrieved image sections of scatterers, we mainly discuss three areas in which seismic and tectonic features appear, because it is hard to interpret all scatterers due to the lack of complete raypath coverage. The selected areas are as follows: (1) along the NRF system, (2) the Shirasawa caldera region, and (3) the coseismic area of the 1998 M_j = 5.2 earthquake. At the surface trace of the NRF, we found that a high *P-S* scattering zone in a frequency range of 8–16 Hz is concentrated at a shallow depth range of −1 km to 2 km (Figure 8b). Around the Shirasawa caldera region, we identified a high *P-P* scattering zone at a depth range of 5–11 km (Figure 8a). Several *P-S* scatterers were also identified in the caldera with large scattering coefficients at a shallow depth range of −1–8 km (Figure 8b). Around the main shock of the 1998 M_j 5.2 earthquake, we did not identify a clustering of scatterers in all the frequency ranges for both *P-P* and *P-S* scatterers at a depth range of 11–14 km (Figures 6, 7, and 8), except a few weak *P-P* scatterers in a frequency range of 8–16 Hz.

[32] We conducted a simple numerical experiment to assess the spatial resolution of scatterers as well as the ability of the data set in this study for distinguishing among scattering modes by using the imaging approach. We simply assume the scattered wave of a Ricker wavelet type, as given below. We assigned two *P-P* and two *P-S* scatterers based on the above features for our data set. In other words, this numerical experiment only focused on the spatial resolution of scatterers in the following three regions: (1) the surface trace of the NRF, (2) the Shirasawa caldera region, (3) the hypocenter of the 1998 M_j 5.2 earthquake. We performed a checkerboard test to examine the spatial resolution of scatterers in the entire model space in three frequency ranges: 2–4 Hz, 4–8 Hz, and 8–16 Hz in Appendix A.

[33] One *P-P* scatterer was placed in the Shirasawa caldera region at 7 km depth and the other at the hypocenter of the 1998 M_j 5.2 earthquake at 12 km depth (Figure 9). On the other hand, one *P-S* scatterer was assigned at the near surface trance of the NRF at 1 km depth and the other in the Shirasawa caldera region at 3 km depth (Figure 9). Since the frequency response of each scatterer is not highly band-limited for actual scattering process [e.g., *Yomogida et al.*, 1997; *Sato and Fehler*, 1998], we do not examine its frequency resolution in our numerical experiment. Each scatterer generates the scattered wave composed of a Ricker wavelet with 12 Hz and with the same amplitude.

[34] Assuming the single isotropic scattering model [e.g., *Sato*, 1977] and a plan wave approximation, we synthesized 3-C seismograms with scattering phases from four point-scatterers for the same 15 sources as the actual data

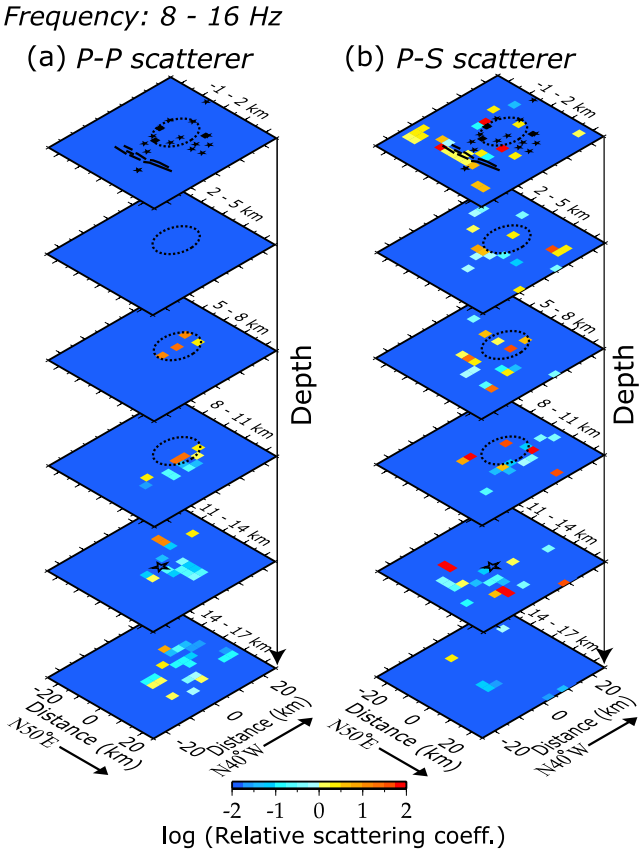

Figure 8. Same as Figure 6 except for 8–16 Hz.

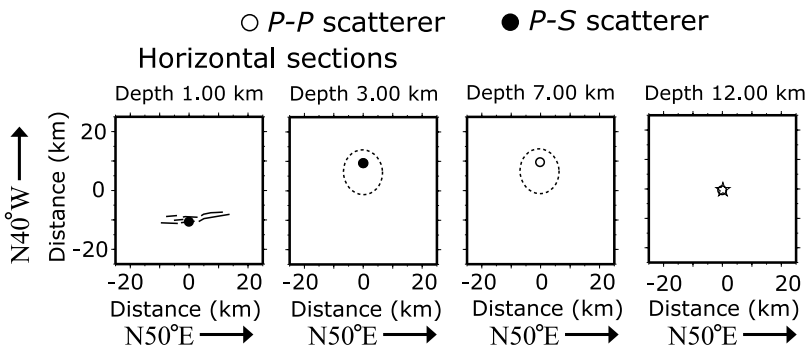

Figure 9. Assigned locations of *P-P* (open circles) and *P-S* (solid circles) scatterers for the numerical experiment in this study. Open star, black lines, and dashed ovals indicate the hypocenter of the 1998 M_j 5.2 earthquake, the surface trace of the NRF system, and the Shirasawa caldera region, respectively.

(Figure 10). Gaussian white noise of 20% of the average signal level were added to the synthetic waveforms. With the actual data, we only analyzed the early coda part where the signal-to-noise ratio is greater than 2, better than our numerical experiments. Although we added simple Gaussian noise, the above factor should not alter our estimation of resolution even if we include more realistic or complex noise. Note that we do not consider any reflections at ground surface. Note also that we assume that displacement of *SV* wave is the same as one of *SH* wave.

[35] Figure 11 shows the result of the present numerical experiment. We normalized *P-P* and *P-S* scattering coefficients by a common value, in order to compare the distributions of scattering coefficients between the two scatterings. In addition, we mapped scatterers inferred from at least two shot-array pairs. The assigned four scatterers were generally well recovered, although spatial extents of several km from placed scatterers appear in image sections. We concluded the spatial resolution of scatterers is high enough for the present scope of imaging.

3.3. Effects of Converted Waves at Ground Surface and Shear Waves From Nonisotropic Source Radiation

[36] Before going into implications of our imaging results on seismic scatterers, it is necessary to evaluate the contribution of the ground surface because we shall neglect it in the rest of this study. We here consider (1) *S-S* and (2) *S-P* scattered phases as the scattered waves from each scatterer with an incident wave to be the *P-S* surface-converted wave, that is, the direct *P*-wave radiated from a very shallow explosion source is converted to *S* wave upon the reflection at a shallow ground surface. The above two types of scattered phases are here called *pS-S* and *pS-P* scatterings, respectively. Note that scattered waves from a *P-P* surface-converted wave (i.e., *P* wave reflected at the surface or *pP-P* or *pP-S* scattering, following the nomenclature adopted above) are not important in this study because their ray parameters and travel times are very similar to the *P* wave incident directly from the source to scatterers, owing to all the present explosion sources located near the ground surface. In addition, large-amplitude *S*-waves are often radiated from explosion sources [e.g., *Hron and Mikhailenko*, 1981; *Lee and Balch*, 1982], and we also need to take into account such a wave, widely called *S**, carefully.

[37] Our imaging method developed in Paper I estimates the precise incident angle of each scattered wave and maps each *f-k* power spectral peak of the detected phase into blocks in the model space within the fit function value greater than 0.95, as mentioned in section 3.1. The travel time of *pS-S* or *S***-S* phase differs from one of *P-S* phase (i.e., the *P* wave incident directly from the source to a scatterer then propagating to the station as *S* wave) by much more than few tenths of a second in general, due to the difference in *P*- and *S*-wave velocities. The calculated travel time for any misinterpreted scattering modes does therefore not satisfy fit function value with greater than 0.95, so that we never map *pS-S* or *S***-S* phase by the present imaging method even if we misinterpret an observed *pS-S* or *S***-S* phase as *P-S* one.

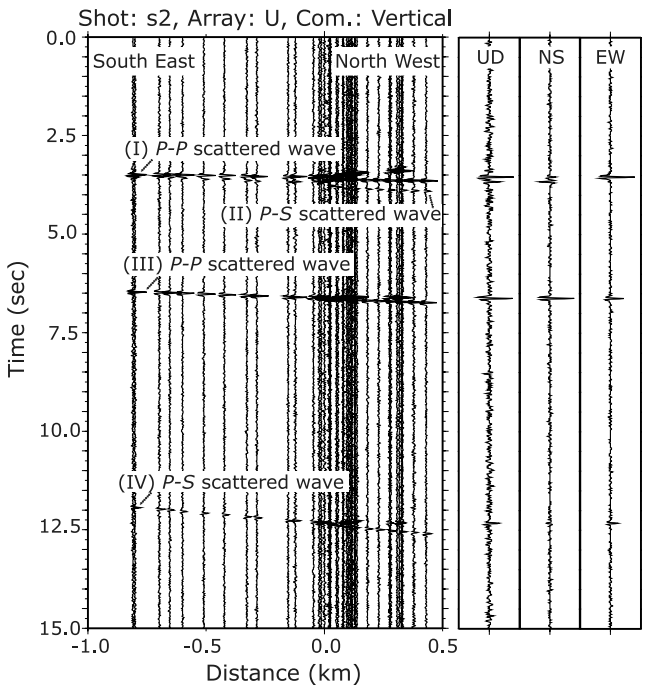

Figure 10. (left) Example of synthetic seismograms for shot s2 at vertical component of array U. (right) Enlarged view of the 3-C seismogram at the reference station, station 6042.

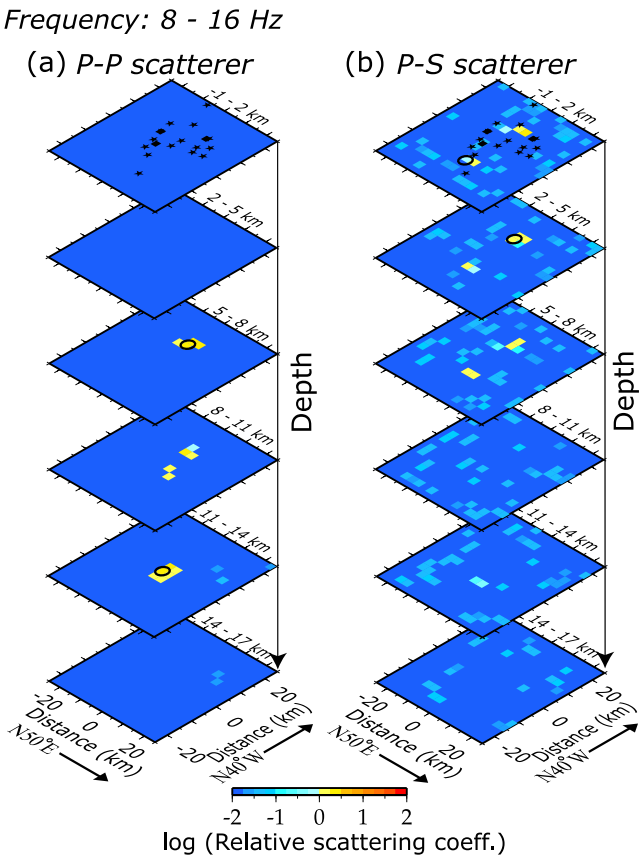

Figure 11. Depth slices of the distributions of scattering coefficients for (a) *P-P* and (b) *P-S* scatterers in a frequency range of 8–16 Hz for the numerical experiment. The magnitude of each relative scattering coefficient is shown by the color bar, as shown at the bottom. The assigned locations of scatterers are shown by the open circles. Solid stars and squares denote shot and array locations, respectively.

[38] It is also easy to remove *pS-P* and *S*-P* phases in a similar manner to *pS-S* phase because their travel times are very different. In addition, we can safely neglect the contribution of *pS-P* and *S*-P* phases in the present imaging result because the amplitude of *S-P* scattering is firmly proved to be negligible compared with one of *S-S* scattering both theoretically and numerically [e.g., *Yomogida et al.*, 1997; *Sato and Fehler*, 1998]. In other words, the amplitude of *pS-P* (or *S*-P*) phase is much smaller than one of *pS-S* (or *S*-S*) phase as well as those of the two phases to be imaged (i.e., *P-P* and *P-S*).

[39] In conclusion, the effect of converted or reflected waves at the ground surface in this study should not alter our final results on the distribution of scattering coefficients severely, mainly owing to (1) the use of not only travel time but also ray parameter or wave number vector estimated by the array processing and (2) very shallow explosion sources.

4. Seismological Implications

4.1. Near the Surface Trace of the NRF

[40] We found that a zone of large *P-S* scattering coefficients in a frequency range of 8–16 Hz is concentrated near the surface trace of the NRF at a shallow depth range of −1 km to 2 km. In contrast, such a high *P-S* scattering zone in a frequency range of 2–4 Hz or 4–8 Hz seems to spread to a certain range of depth at the same spot. As discussed with the resolution test in Appendix A (see Figures A3, A4, and A5 in Appendix A), we have high spatial horizontal resolutions for *P-S* scattering in all the frequency ranges at depth shallower than 5 km except for a few scatterers. These clear frequency dependencies of *P-S* scattering suggest different distributions of heterogeneities in size around the surface trace of the fault. The existence of very shallow scatterers at the surface trace of the fault is probably due to geological features such as a boundary between sedimentary and basement morphologies.

[41] *Yomogida et al.* [1998] studied scattered waves by localized heterogeneities with numerical simulations, focusing on the spatial variation of coda level relative to focal depth in media where heterogeneities are localized within a certain depth range. They suggested that notable local amplification of coda level takes place only in a particular frequency range in which the scattering effect is the strongest: the non-dimensional frequency *kd*, (wave number of each scattered wave) × (size of each heterogeneity), is about 2.

[42] Assuming the shear wave velocity at 1.5 km depth to be 3.06 km/s [*Imanishi et al.*, 2002], the corresponding scale of small-scale heterogeneities is estimated to be about 0.08 km, using the dominant frequency of scattered waves to be 12 Hz. Since strong scattering can be associated with fractures concentrated there, the obtained high scattering zone should correspond to an area of highly concentrated heterogeneities of the fracture size around 0.08 km. Note that we cannot estimate the size of small-scale heterogeneities much smaller than 0.08 km because we analyzed the seismograms of frequency lower than 16 Hz.

[43] Another important feature of the image sections of scatterers is the absence of *P-P* scattering around surface trace of the fault. The dependence of scattering mode can be attributed to the perturbation of elastic modulus and density [*Sato and Fehler*, 1998]. *O'Connell and Budiansky* [1974] summarized fluctuations of elastic modulus associated with variations of the degree of saturation in cracks, showing that shear modulus is more sensitive to the degree of saturation than bulk modulus. We therefore suggest that the high *P-S* scattering near the surface trace of the fault is characterized by fluid-filled cracks or fractures, although *S-P* and *S-S* scattering coefficients were not evaluated in this study. We are currently extending our method to estimate scattering coefficients with all the scattering modes (i.e., *P-P*, *P-S*, *S-P*, and *S-S*), by incorporating seismograms for natural earthquakes.

4.2. Shirasawa Caldera

[44] One remarkable feature of *P-P* scattering is identified in the northwest of the NRF at a depth range of 5–11 km, corresponding to the Shirasawa caldera region [*Yoshida*, 2001]. In particular, *P-P* scatterers in a frequency range of 8–16 Hz is much more dominant than one in another frequency range. (Figure 8a). As mentioned in Appendix A, we cannot retrieve assigned scatterers near the caldera area at depth shallower than 5 km in frequency ranges of 2–4 Hz and 4–8 Hz (Figures A3 and A4 in Appendix A).

Imanishi et al. [2002] analyzed the 5 Hz to 15 Hz bandpass-filtered seismograms recorded by four small-aperture arrays, including arrays A and C for the same explosion sources. They estimated the location and intensity of scatterers around the NRF, indicating a high scattering zone near the caldera, assuming them as *P-P* scattering mode. The area of high *P-P* scattering detected in this study is consistent with the above previous result in terms of not only its location but also the dominant frequency and scattering mode of scattered phases.

[45] Assuming *P*-wave velocity at 8 km depth to be 6.0 km/s [*Imanishi et al.*, 2002], the heterogeneous scale length of the *P-P* scattering area is estimated to be about 0.16 km, using the relationship between the scale length of heterogeneity and the dominant frequency of the detected scattered wave [*Yomogida et al.*, 1998], as mentioned in the previous section. In addition to the scale length, we suggest that this high *P-P* scattering area can be attributed to crustal heterogeneity associated with plutons, because the caldera at the depth of midcrust is characterized by unexposed plutons [*Yoshida*, 2001].

[46] We also detected several *P-S* scatterers in the caldera with large scattering coefficients at a shallow range of −1−8 km deep in all frequency ranges (Figures 6b, 7b, and 8b), although they are not localized. Note that since both spatial resolutions for *P-P* and *P-S* scatterers in a frequency ranges of 8−16 Hz are better than those in the other two frequency ranges (Figures A3, A4, and A5 in Appendix A), we discuss characteristics of image sections in a frequency range of 8−16 Hz. Combining the obtained *P-P* and *P-S* scatterers distributions, one important feature of the caldera in terms of crustal scattering is that the dominant scattering mode seems to change from *P-S* to *P-P* around the caldera, as depth increases. In other words, *P-P* scatterers tend to be localized at depth deeper than 5 km, while *P-S* scatterers at depth shallower than around 8 km.

[47] Since the scattered waves can be generated by the perturbation or heterogeneous distribution of elastic properties in the medium [e.g., *Aki and Richards*, 1980], we suppose that this systematic variation with depth is mainly caused by large fluctuations of elastic properties in the medium, and it is natural to consider that such large fluctuations imply the existence of many cracks or fractures. The above feature, therefore, implies that the materials composed of seismic scatterers may change fluid-fill cracks in shallow to dry cracks in deep because *P-S* scattering becomes relatively effective in the case of fluid-fill cracks [e.g., *O'Connell and Budiansky*, 1974].

[48] *Takei* [2002] attempted to constrain physical status in the Earth's interior, using V_p/V_s velocity ratio estimated by seismic tomography. She proposed the equivalent aspect ratio representing pore geometries (e.g., crack or tube models), showing that V_p/V_s velocity ratio depends on not only liquid compressibility but also pore geometry. Although we must be careful of the selection of the adopted model of scatterers (i.e., cracks) or fluctuation of seismic velocity, together with the surrounding condition of pressure and temperature, the ratio of *P-P* to *P-S* scattering coefficients may constrain physical properties of seismic scatterers effectively, in the similar manner to *O'Connell and Budiansky* [1974] and *Takei* [2002]. The ratio of relative scattering coefficients may help us to quantify the modeling of seismic scatterers because the existence of fluid (i.e., nearly zero *S*-wave velocity but finite *P*-wave velocity) inside a scatterer should be more effective for *P-S* scattering than *P-P* scattering, compared with one filled with solid materials of low velocity. It is, however, difficult to make any systematic comparison between *P-P* and *P-S* scattering coefficients in this study because both *P-P* and *P-S* scattering coefficients are reliably obtained only for a few model blocks. More reliable images to these two maps (i.e., *P-P* and *P-S*) should be obtained in future, and it will be preferable to introduce images for not only these values but also the ratio of *P-P* versus *P-S* scatterings for future constraint on the properties of scatterers.

4.3. Around the Main Shock of the 1998 M_j 5.2 Earthquake

[49] Detecting crustal heterogeneities in an active fault system is one of the key aspects of the nucleation process of earthquakes because these crustal heterogeneities can be highly sensitive to the stress state within a seismogenic zone where stress is accumulated. Some studies reported that a subhorizontal detachment exists in deep extension of some active faults, using scattered waves associated with heterogeneities [e.g., *Nishigami*, 2000].

[50] Several studies interpreted a weak scattering area as a locked segment in a fault zone. *Nishigami* [2000] estimated the 3-D distribution of *S-S* scattering coefficients in the crust along and around the San Andreas fault system in central California, using an inversion analysis of coda envelopes. He suggested that a zone of weak scattering is most likely to correspond to the ruptured areas of several former earthquakes with magnitude larger than 6 along the fault system.

[51] As mentioned in section 2.1, a moderate earthquake with M_j 5.2 occurred at the deepest portion of the NRF on 15 September 1998. The fault plane of the 1998 M_j 5.2 earthquake is dipping northwest with an angle of about 30° and its size of approximately 3 km × 3 km [*Okada et al.*, 2001]. Since the block size representing scattering coefficients is 3 km × 3 km × 3 km in this paper, the block placed at center of the model space and at 12 km depth corresponds to the entire coseismic area of the 1998 M_j 5.2 earthquake. As shown in Figure 11 and in Figures A3, A4, and A5 in Appendix A, we have good spatial resolutions for *P-P* and *P-S* scatterers, particularly in a frequency range of 8−16 Hz to distinguish them.

[52] A clustering of scatterers at the coseismic area of the 1998 M_j 5.2 earthquake is not detected here in all the frequency ranges for both *P-P* and *P-S* scatterers at a depth range of 11−14 km (Figures 6, 7, and 8), except a few weak *P-P* scatterers in a frequency range of 8−16 Hz. Similar to the result of *Nishigami* [2000], there appear to exist a zone of weak scattering coefficients that may correspond to a locked segment of the deepest portion of the NRF. This result implies that a locked segment can store high stress probably owing to its relatively homogeneous nature, so that this portion has potential to generate a relatively large earthquake, compared with its adjacent portions of the fault.

[53] Nevertheless, one may need to be careful of the difference in depth range of coseismic areas between the Nagamachi-Rifu and the San Andreas faults. The majority of coseismic slips in the San Andreas fault, a strike-slip fault, took place at depth shallower than 12 km [*Bakun*, 1998]. In

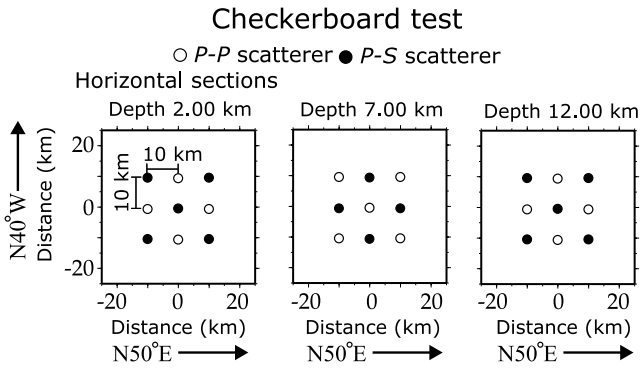

Figure A1. A checkerboard pattern with *P-P* (open circles) and *P-S* (solid circles) scatterers.

contrast, the coseismic area of the 1998 M_j 5.2 earthquake of the NRF, a low-angle thrust fault, are located at the depth of about 12 km. A part of local stress deeper than 10 km should be released by fault creep around the NRF. *Nishimura et al.* [2001] showed quasi-static sliding at the deepest portion of the NRF, by using GPS data. The lack of any significant strong scatterers at the coseismic area of the 1998 M_j 5.2 earthquake may be not only due to its homogeneous nature but also some degrees of stress release by fault creep.

[54] As mentioned in section 4.1, *P-S* scatterers are mainly associated with fluid-filled fractures. Fluids at seismogenic zone play an important role in the nucleation process of earthquakes, it is important to monitor spatial and temporal changes in scatterers. *Niu et al.* [2003] found a systematic temporal variation in coda arrivals from repeating earthquakes around the Parkfield segment of San Andreas Fault, showing a shift of the order of 0.01 km in the location of a specific scatterer. They suggested that this temporal change should be the result of a stress-induced redistribution of fluid in fluid-filled fractures caused by the 1993 aseismic transient event. We are currently developing a scatterer-imaging methodology to investigate spatiotemporal variations of scatterers.

5. Conclusions

[55] We applied the imaging approach developed in Paper I to the seismic data recorded around the NRF, northeastern Japan. We revealed that small-scale heterogeneities in this area are distributed not only with different scale lengths (i.e., frequencies) but also with different scattering modes (i.e, *P-P* versus *P-S* scatterings). We focused the following three areas that are interesting in seismological and tectonic points of view, taking advantages of the improved imaging results in this study.

[56] 1. There are concentrations only for *P-S* scatterers near the surface trace of the NRF. This fault area of large scattering coefficients implies the existence of the abundance of fractures with their sizes around or smaller than 0.08 km, based on the dominant frequency. The strong *P-S* scattering with the weak *P-P* scattering implies that the heterogeneities in the area are associated with fluid-filled fractures.

[57] 2. Another area of large relative scattering coefficients is found in the northwest of the NRF at depth shallower than 11 km, where an old caldera, named Shirasawa Caldera, is supposed to exist. As depth increases, the dominant seismic scattering mode changes from *P-S* to *P-P*. The above depth-dependent feature of scattering implies that the materials composed of seismic scatterers may change from fluid-fill to dry cracks with increasing depth.

[58] 3. Scattering coefficients are not anomalous around the coseismic area of the 1998 M_j 5.2 earthquake. In other words, such a zone of rather weak scattering, or a relatively homogeneous zone appears to correspond to a locked segment of the NRF. This part may have potential to produce a large earthquake because a locked segment can store relatively high stress. There are several previous studies which interpret an area of weak scattering as a locked segment in an active fault system [*Nishigami*, 2000].

[59] Further studies including more complex phenomena, such as nonisotropic and multiple scattering, will reveal more physical insight into the materials and physical properties of small-scale heterogeneities. For this purpose, we need to utilize observations with multiple arrays fully, together with more advanced models of scattering processes.

Appendix A: Numerical Simulation

[60] To examine not only the spatial resolution of image sections but also the ability of our data set for distinguishing among scattering modes, we performed a checkerboard test, which has been widely adopted for travel time tomography as well as some previous imagings of scattering coefficients [e.g., *Chen and Long*, 2000]. We simply assume the scattered wave of a Ricker wavelet type, as given below.

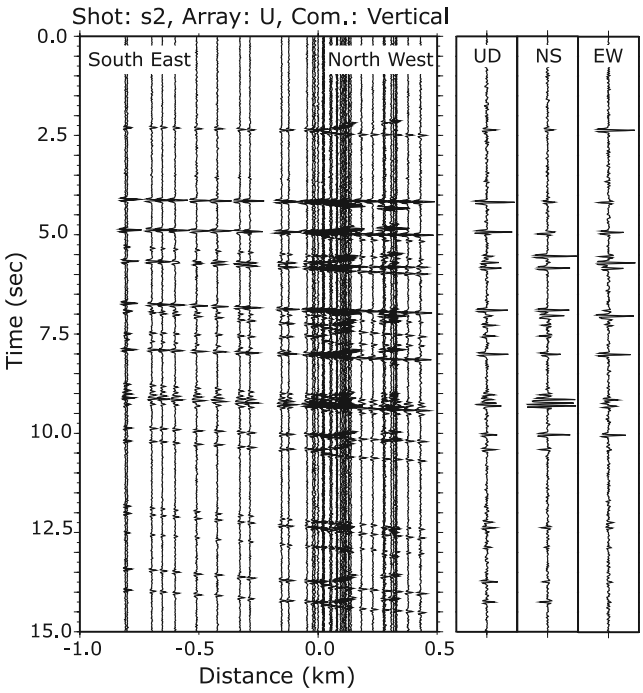

Figure A2. (left) Example of synthetic seismograms with 12 Hz Ricker wavelets for shot s2 at vertical component of array U. (right) Enlarged view of the 3-C seismogram at the reference station, station 6042.

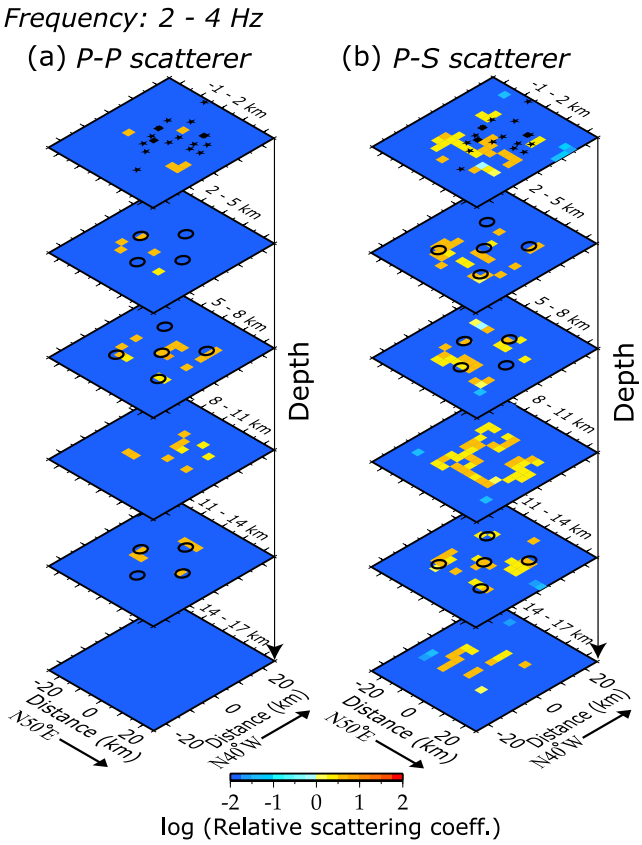

Figure A3. Depth slices of the distributions of scattering coefficients for (a) *P-P* and (b) *P-S* scatterers in a frequency range of 2–4 Hz for the checkerboard test. The magnitude of each relative scattering coefficient is shown by the color bar, as shown at the bottom. The assigned locations of scatterers are shown by the open circles. Solid stars and squares denote shot and array locations, respectively.

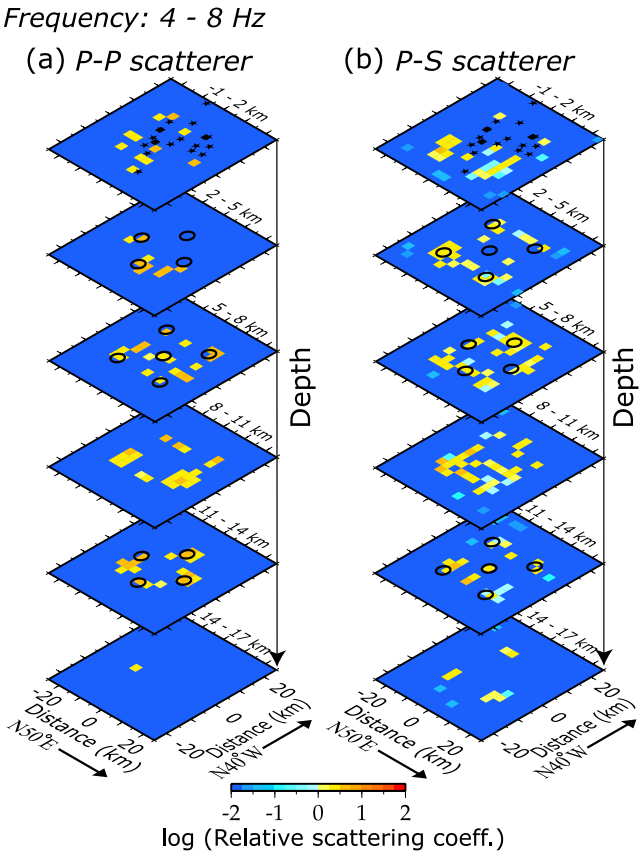

Figure A4. Same as Figure A3 except for 4–8 Hz.

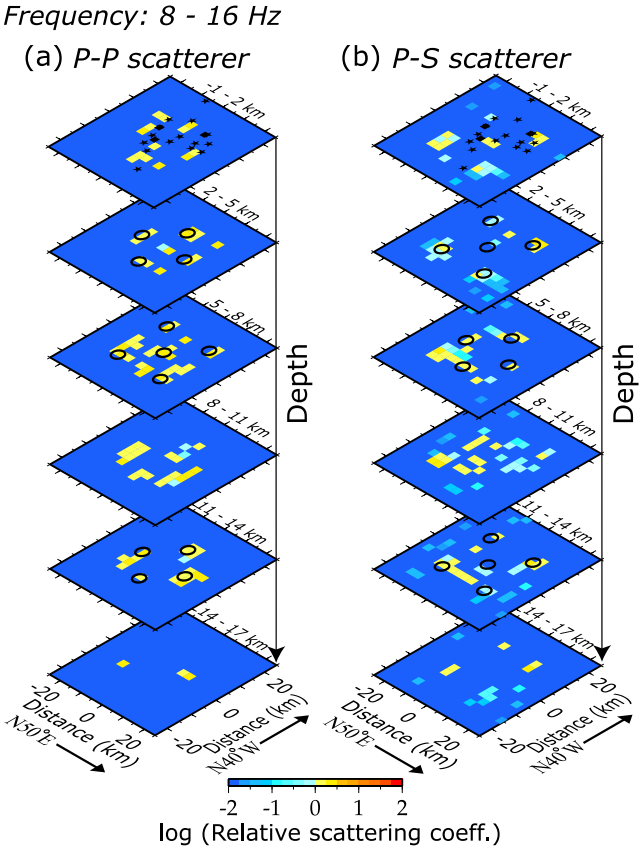

Figure A5. Same as Figure A3 except for 8–16 Hz.

We assigned 13 *P-P* and 14 *P-S* scatterers alternately, and these two kinds of scatterers are arranged in the interval of 10 km in horizontal and 5 km in depth in the model space (Figure A1). Each scatterer generates the scattered wave composed of a Ricker wavelet with a given central frequency (i.e., 3 Hz, 6 Hz, and 12 Hz) and with the same amplitude. We synthesized 3-C seismograms with scattered phases, given a central frequency, from 27 point-scatterers for the same 15 sources as the actual data (Figure A2), assuming the single isotropic scattering model [e.g., *Sato*, 1977] with a plan wave approximation. Gaussian white noise of 20% of the average signal level as added to the synthetic waveforms.

[61] Figures A3, A4, and A5 show the results of the present resolution test in three frequency ranges of 2–4 Hz, 4–8 Hz, and 8–16 Hz, respectively. We normalized *P-P* and *P-S* scattering coefficients in all the frequency ranges by a common value. We mapped scatterers inferred from at least two shot-array pairs.

[62] We found that scatterers were generally well recovered, although spatial extents of 3–5 km from placed scatterers appear in image sections. In addition, the assigned patterns of scattering coefficients were not fully reconstructed in some parts, for example, in a frequency range of

2–4 Hz, *P-P* scatterer at a depth range of 2–5 km due to some scattered waves arriving more simultaneously at a certain time more at low frequency. Nevertheless, the overall resolution is sufficient for the present scope of imaging even in a low-frequency case. In the interpretation of the distributions of scattering coefficients in section 4, these features of resolution must be taken into consideration.

[63] **Acknowledgments.** We thank Junji Koyama, Takeo Moriya, Tsutomu Sasatani, Tetsuo Takanami, and Kazunori Yoshizawa at Hokkaido University for their valuable and helpful advice and suggestions. We appreciate the Research Group for Deep Structure of Nagamachi Rifu Fault and Geological Survey of Japan, National Institute of Advanced Industrial Science and Technology, for permission to use their seismic waveform data and to the members of its analyzing committee for the preparation of the data ready to be analyzed. These observations were conducted as a part of the Comprehensive Research on Slip and Flow Processes in and below the Seismogenic Region supported by the Special Coordination Fund of the Ministry of Education, Culture, Sports, Science, and Technology. We also thank Junichi Nakajima at Tohoku University to provide us with 3-D seismic velocity structures around the Nagamachi-Rifu fault. Valuable comments by Justin Revenaugh at University of Minnesota, Charles K. Wilson at Lamont-Doherty Earth Observatory of Columbia University, and anonymous reviewers are greatly appreciated. A software package, Generic Mapping Tools (GMT) [*Wessel and Smith*, 1995] was used to plot some figures. This work was partially supported by the Earthquake Research Institute Cooperative Research Programs (2000-B-07, 2001-B-02, and 2003-B-04). The second author (K. Y.) was also supported in part by the bilateral treaty between the Royal Society and Japan Society of Promotion of Science.

References

Active Fault Research Group (1991), *Active Faults in Japan: Sheet Maps and Inventories*, rev. ed., Univ. of Tokyo Press, Tokyo.

Aki, K. (1969), Analysis of seismic coda of local earthquakes as scattered waves, *J. Geophys. Res.*, *74*, 615–631.

Aki, K. (1973), Scattering of *P* waves under the Montana Lasa, *J. Geophys. Res.*, *78*, 1334–1346.

Aki, K. (1982), Scattering and attenuation, *Bull. Soil Soc. Am.*, *72*, 5319–5330.

Aki, K. (1992), Scattering conversions P to S versus S to P, *Bull. Soil Soc. Am.*, *82*, 1969–1972.

Aki, K., and P. G. Richards (1980), *Quantitative Seismology, Theory and Methods*, W.H. Freeman, San Francisco, Calif.

Bakun, W. H. (1998), Scenarios for historic San Francisco Bay region earthquakes, *U. S. Geol. Surv. Open File Rep.*, 98–785.

Bannister, S. C., E. S. Husebye, and B. O. Ruud (1990), Teleseismic P coda analyzed by three-component and array technique: Deterministic location of topographic P-to-Rg scattering near the NORESS array, *Bull. Soil Soc. Am.*, *80*, 1969–1986.

Capon, J. (1969), High-resolution frequency-wavenumber spectrum analysis, *Proc. IEEE*, *57*, 1408–1418.

Capon, J. (1974), Characterization of crust and upper mantle structure under Lasa as a random medium, *Bull. Soil Soc. Am.*, *64*, 235–266.

Chen, X., and L. T. Long (2000), Spatial distribution of relative scattering coefficients determined from microearthquake coda, *Bull. Soil Soc. Am.*, *90*, 512–524.

Frankel, A., S. Hough, P. Friberg, and R. Busby (1991), Observation of Loma Prieta aftershocks from a dense array in Sunnyvale, California, *Bull. Soil Soc. Am.*, *80*, 1900–1922.

Frederiksen, A. W., and J. Revenaugh (2004), Lithospheric imaging via teleseismic scattering tomography, *Geophys. J. Int.*, *159*(3), 978–990, doi: 10.1111/j.1365-246X.2004.02414.x.

Hasegawa, A., H. Ito, T. Iwasaki, and T. Ikawa (2001), Deep structure of Nagamachi-Rifu fault as inferred from seismic expeditions, paper presented at International Symposium on Slip and Flow Processes In and Below the Seismogenic Region, Min. of Educ., Culture, Sports, Sci. and Technol., Sendai, Japan.

Hron, F., and B. G. Mikhailenko (1981), Numerical modeling of nongeometrical effects by the Alekseev-Mikhailenko method, *Bull. Soil Soc. Am.*, *71*, 1011–1029.

Ikawa, T., T. Kawanaka, S. Kawasaki, A. Hasegawa, N. Umino, A. Nakamura, H. Ito, T. Iwasaki, and H. Sato (2001), Seismic reflection survey of the deep structure of Nagamachi-Rifu fault, northeastern Japan, paper presented at International Symposium on Slip and Flow Processes In and Below the Seismogenic Region, Min. of Educ., Culture, Sports, Sci. and Technol., Sendai, Japan.

Imanishi, K., H. Ito, Y. Kuwahara, Y. Mamada, T. Yokokura, N. Kano, K. Yamaguchi, and A. Tanaka (2002), Deep structure of the Nagamachi-Rifu fault deduced from small aperture seismic array observations, *Earth Planets Space*, *54*, 1033–1038.

Kaneshima, S., and G. Helffrich (1998), Detection of lower mantle scatterers northeast of the Marianna subduction zone using short-period array data, *J. Geophys. Res.*, *103*, 4825–4838.

Krüger, G., M. Weber, F. Scherbaum, and J. Schlittenhardt (1993), Double beam analysis of anomalies in the core-mantle boundary region, *Geophys. Res. Lett.*, *20*, 1475–1478.

Lee, M. W., and A. H. Balch (1982), Theoretical seismic wave radiation from a fluid-filled borehole, *Geophysics*, *47*, 1308–1314.

Louie, J. N., S. Chávez-Pérez, S. Henrys, and S. Bannister (2002), Multimode migration of scattered and converted waves for the structure of the Hikurangi slab interface, New Zealand, *Tectonophysics*, *335*, 225–246.

Miyagi Prefectural Government, Research on the Nagamachi-Rifu fault (1997), Abstract for the results of active fault research supported by Headquarters for Earthquake Research Promotion (in Japanese), *Rep. 1*, pp. 30–34, Sci. and Technol. Agency, Saitama, Japan.

Nakajima, J., A. Hasegawa, S. Horiuchi, K. Yoshimoto, T. Yoshida, and N. Umino (2006), Crustal heterogeneity around the Nagamachi-Rifu fault, northeastern Japan, as inferred from travel-time tomography, *Earth Planets Space*, *58*, 843–853.

Nakamura, A., Y. Asano, and A. Hasegawa (2002), Estimation of deep fault geometry of the Nagamachi-Rifu fault from seismic array observation, *Earth Planets Space*, *54*, 1027–1031.

Neidell, N. S., and M. T. Taner (1971), Semblance and other coherency measures for multichannel data, *Geophysics*, *36*, 482–497.

Nishigami, K. (2000), Deep structure heterogeneity along and around the San Andreas fault system in central California and its relation to the segmentation, *J. Geophys. Res.*, *105*, 7983–7998.

Nishimura, T., T. Sagiya, T. Tada, and S. Miura (2001), High strain rate west of the Nagamachi-Rifu fault, northeastern Japan, observed by a dense GPS array, paper presented at International Symposium on Slip and Flow Processes In and Below the Seismogenic Region, Min. of Educ., Culture, Sports, Sci. and Technol., Sendai, Japan.

Niu, F., P. G. Silver, R. M. Nadeau, and T. V. McEvilly (2003), Migration of seismic scatterers associated with the 1993 Parkfield aseismic transient event, *Nature*, *426*, 544–548.

O'Connell, R. J., and B. Budiansky (1974), Seismic velocities in dry and saturated cracked solids, *J. Geophys. Res.*, *79*, 5412–5426.

Okada, T., N. Umino, Y. Ito, T. Matsuzawa, A. Hasegawa, and M. Kamiyama (2001), Source processes of 15 September 1998 M 5.0 Sendai, northeastern Japan, earthquake and its M 3.8 foreshock by waveform inversion, *Bull. Soil Soc. Am.*, *91*, 1607–1618.

Research Group for Deep Structure of Nagamachi-Rifu Fault (2002), Seismic reflection survey in Nagamachi-Rifu fault, Sendai, northeastern Japan, *Tohoku Geophys. J.*, *36*, 311–356.

Revenaugh, J. (1995), A scattered-wave image of subduction beneath the Transverse Range, *Science*, *268*, 1888–1892.

Revenaugh, J. (2000), The relation of crustal scattering to seismicity in southern California, *J. Geophys. Res.*, *105*, 25,403–25,422.

Rietbrock, A., and F. Scherbaum (1999), Crustal scattering at the KTB from a combined microearthquake and receiver analysis, *Geophys. J. Int.*, *136*(1), 57–67, doi:10.1046/j.1365-246X.1999.00708.x.

Rondenay, S., M. G. Bostock, and J. Shragge (2001), Multiparameter two-dimensional inversion of scattered teleseismic body waves: 3. Application to the Cascadia 1993 data set, *J. Geophys. Res.*, *106*, 30,795–30,807.

Rothert, E., and J. R. R. Ritter (2001), Small-scale heterogeneities below the Gräfenberg array, Germany, from seismic wavefield fluctuations of Hindu Kush events, *Geophys. J. Int.*, *140*, 175–184.

Sato, H. (1977), Energy propagation including scattering effects: Single isotropic scattering approximation, *J. Phys. Earth*, *25*, 27–41.

Sato, H. (1994), The relationship between late Cenozoic tectonic events and stress field and basin development in northeast Japan, *J. Geophys. Res.*, *99*, 22,261–22,274.

Sato, H., and M. C. Fehler (1998), *Seismic Wave Propagation and Scattering in the Heterogeneous Earth*, Springer, New York.

Sato, H., T. Imaizumi, T. Yoshida, H. Ito, and A. Hasegawa (2002), Tectonic evolution and deep to shallow geometry of Nagamachi-Rifu active fault system, NE Japan, *Earth Planets Space*, *54*, 1039–1043.

Scherbaum, F., F. Krüger, and M. Weber (1997), Double beam imaging: Mapping lower mantle heterogeneities using combinations of source and receiver arrays, *J. Geophys. Res.*, *102*, 507–522.

Spudich, P., and T. Bostwick (1987), Studies of the seismic coda using an earthquake cluster as a deeply buried seismograph array, *J. Geophys. Res.*, *92*, 10,526–10,546.

Taira, T., and K. Yomogida (2004), Imaging of three-dimensional small-scale heterogeneities in the Hidaka, Japan, region: Coda spectral analysis, *Geophys. J. Int.*, *158*(3), 998–1008, doi:10.1111/j.1356-246X.2004.02333.x.

Taira, T., and K. Yomogida (2007), Imaging of crustal heterogeneous structures using a slowness-weighted back-projection with effects of scattering modes: 1. Theory, *J. Geophys. Res.*, doi:10.1029/2006JB004381, in press.

Takei, Y. (2002), Effect of pore geometry of V_p/V_s: From equilibrium geometry to crack, *J. Geophys. Res.*, *107*(B2), 2043, doi:10.1029/2001JB000522.

Um, J., and C. Thurber (1987), A fast algorithm for 2-point seismic ray tracing, *Bull. Soil Soc. Am.*, *77*, 972–986.

Umino, N., T. Okada, and A. Hasegawa (2002a), Foreshock and aftershock sequence of 1998 M5.0 Sendai, northeastern Japan, earthquake and its implications for earthquake nucleation, *Bull. Soil Soc. Am.*, *92*, 2465–2477.

Umino, N., H. Ujikawa, S. Hori, and A. Hasegawa (2002b), Distinct S-wave reflectors (blight spots) detected beneath the Nagamachi-Rifu fault, NE Japan, *Earth Planets Space*, *54*, 1021–1026.

Wessel, P., and W. H. F. Smith (1995), New version of the Generic Mapping Tools released, *Eos Trans. AGU*, *76*, 329.

Wu, R. S., and K. Aki (1985), Elastic wave scattering by a random medium and the small scale inhomogeneities in the lithosphere, *J. Geophys. Res.*, *90*, 10,261–10,273.

Yomogida, K., R. Benites, P. M. Roberts, and M. Fehler (1997), Scattering of elastic waves in 2-D composite media II. Waveforms and spectra, *Phys. Earth Planet. Inter.*, *104*, 175–192.

Yomogida, K., R. Benites, and R. Robinson (1998), Spatial variation of coda wave amplitude in media with a localized heterogeneous region, *Earth Planets Space*, *50*, 303–312.

Yoshida, T. (2001), The evolution of arc magmatism in the NE Honshu arc, Japan, *Tohoku Geophys. J.*, *36*, 131–149.

Yoshimoto, K., N. Uchida, H. Sato, M. Ohtake, N. Hirata, and K. Obara (2000), Microseismisity around the Nagamachi-Rifu fault, Miyagi prefecture, northeastern Japan (in Japanese with English abstract), *J. Seismol. Soc. Jpn.*, *52*, 407–416.

K. Imanishi and Y. Kuwahara, Geological Survey of Japan, National Institute of Advanced Industrial Science and Technology, Tsukuba 305-8567, Japan. (imani@ni.aist.go.jp; y-kuwahara@aist.go.jp)

H. Ito, Center for Deep Earth Exploration, Japan Agency for Marine-Earth Science and Technology, Yokohama 236-0001, Japan. (hisaoito@jamstec.go.jp)

T. Taira, Department of Terrestrial Magnetism, Carnegie Institution of Washington, Washington, DC 20015, USA. (taira@dtm.ciw.edu)

K. Yomogida, Division of Earth and Planetary Sciences, Graduate School of Science, Hokkaido University, Sapporo 060-0810, Japan. (yomo@mail.sci.hokudai.ac.jp)